Computers in Biology and Medicine 162 (2023) 107073

Contents lists available at ScienceDirect

Computers in Biology and Medicine

journal homepage: www.elsevier.com/locate/compbiomed

Simulation of a new respiratory phase sorting method for 4D-imaging using optical surface information towards precision radiotherapy

Zhengkun Dong [a,b,1], Shutong Yu [a,b,1], Adam Szmul [c], Jingyuan Wang [d], Junfeng Qi [e], Hao Wu [a], Junyu Li [a], Zihong Lu [a], Yibao Zhang [a,*]

[a] Key Laboratory of Carcinogenesis and Translational Research (Ministry of Education/Beijing), Department of Radiation Oncology, Peking University Cancer Hospital & Institute, Beijing, 100142, China
[b] Institute of Medical Technology, Peking University Health Science Center, Beijing, 100191, China
[c] Wellcome/EPSRC Centre for Interventional and Surgical Sciences, University College London, London, United Kingdom
[d] Department of Biostatistics, School of Public Health, Peking University, Beijing, China
[e] Department of Engineering Physics, Tsinghua University, Beijing, 100084, China

ARTICLE INFO

Keywords:
Precision radiotherapy
4D image
Optical surface imaging
Motion management

ABSTRACT

Background: Respiratory signal detection is critical for 4-dimensional (4D) imaging. This study proposes and evaluates a novel phase sorting method using optical surface imaging (OSI), aiming to improve the precision of radiotherapy.

Method: Based on 4D Extended Cardiac-Torso (XCAT) digital phantom, OSI in point cloud format was generated from the body segmentation, and image projections were simulated using the geometries of Varian 4D kV cone-beam-CT (CBCT). Respiratory signals were extracted respectively from the segmented diaphragm image (reference method) and OSI respectively, where Gaussian Mixture Model and Principal Component Analysis (PCA) were used for image registration and dimension reduction respectively. Breathing frequencies were compared using Fast-Fourier-Transform. Consistency of 4DCBCT images reconstructed using Maximum Likelihood Expectation Maximization algorithm was also evaluated quantitatively, where high consistency can be suggested by lower Root-Mean-Square-Error (RMSE), Structural-Similarity-Index (SSIM) value closer to 1, and larger Peak-Signal-To-Noise-Ratio (PSNR) respectively.

Results: High consistency of breathing frequencies was observed between the diaphragm-based (0.232 Hz) and OSI-based (0.251 Hz) signals, with a slight discrepancy of 0.019Hz. Using end of expiration (EOE) and end of inspiration (EOI) phases as examples, the mean±1SD values of the 80 transverse, 100 coronal and 120 sagittal planes were 0.967, 0,972, 0.974 (SSIM); 1.657 ± 0.368, 1.464 ± 0.104, 1.479 ± 0.297 (RMSE); and 40.501 ± 1.737, 41.532 ± 1.464, 41.553 ± 1.910 (PSNR) for the EOE; and 0.969, 0.973, 0.973 (SSIM); 1.686 ± 0.278, 1.422 ± 0.089, 1.489 ± 0.238 (RMSE); and 40.535 ± 1.539, 41.605 ± 0.534, 41.401 ± 1.496 (PSNR) for EOI respectively.

Conclusions: This work proposed and evaluated a novel respiratory phase sorting approach for 4D imaging using optical surface signals, which can potentially be applied to precision radiotherapy. Its potential advantages were non-ionizing, non-invasive, non-contact, and more compatible with various anatomic regions and treatment/imaging systems.

1. Introduction

For thoracic and abdominal cancer patients undergoing radiotherapy, respiratory motion is the leading challenge of accurate dose delivery. Hence, 4-dimensional (4D) images are often acquired to assess the trajectories of targets and organs-at-risk (OARs) during treatment planning and setup guidance. For 4D image reconstruction such as 4D computed tomography (4DCT), 4D magnetic resonance imaging (4DMRI), or 4D cone beam CT (4DCBCT), it is necessary to sort the original images to various respiratory phases, usually based on the

* Corresponding author.
E-mail address: zhangyibao@pku.edu.cn (Y. Zhang).
[1] Zhengkun Dong and Shutong Yu contributed equally to this work.

https://doi.org/10.1016/j.compbiomed.2023.107073
Received 10 February 2023; Received in revised form 9 May 2023; Accepted 27 May 2023
Available online 27 May 2023

Table 1
Geometric parameters of Varian kV CBCT system, based on which image projections were simulated using XCAT phantom to reconstruct 4D CBCTs.

Parameters	Settings
Scanning mode	Half fan
Source to detector distance	1500 mm
Distance from the source to the axis of rotation	1000 mm
Offset of detector	148 mm
Size of detector	1024 mm × 768 mm
Reconstructed image size	512 × 512 × 50
Reconstruct voxel size	0.75 mm × 0.75 mm × 2 mm
The number of projections	1320
Rotation	Circular trajectory, 360°

motion amplitude. Several sorting approaches have been developed, either based on fiducial marker (FM) [1], diaphragm image segmentation [2], external pressure detection [3], or infrared marker block tracking in the anterior-posterior (A-P) direction [4].

As an invasive approach, the application of FM is limited by possible geometric migration [5] and various clinical contraindications such as coagulation disorders and pneumothoraxes [6]. Diaphragm-based sorting is reliable, yet is not applicable when the field-of-view (FOV) cannot cover the diaphragm, or when an enlarged FOV may expose too much of healthy tissue to unnecessary radiation, such as 4D imaging of upper thoracic region or fan beam CT scanning. In addition, respiratory-gated treatment based on FM or diaphragm involves extra imaging dose (X-ray fluoroscopy) or additional hardware integration (magnetic resonance imaging or radio frequency system). The existing external surrogates simplify the complex respiratory motion and anatomic distortion to 1D signal extracted from pressure change or block displacement, which also require contact devices that may interfere with the treatment delivery [3,4].

Recently, optical surface imaging (OSI) has been clinically applied to assist patient positioning and motion management for radiotherapy, improving the setup accuracy and workflow [7]. Commercial OSI systems typically use a combination of light projectors and optical cameras, or a combination of depth camera and infrared laser projector [8,9]. The camera captures patterns of specific textures from the projections on the patient's skin to reconstruct surface images nearly in real-time. Compared with the 1D signals detected from pressure change or block tracking, the OSI provides more informative 4D surface data with high temporal and spatial resolution [10,11]. Therefore, OSI is potentially applicable to sort the respiratory phases if acquired simultaneously with other 4D imaging modalities, as an alternative non-ionizing and contactless approach, which has not been reported in the literature.

To help precision radiotherapy, this work aims to: 1. Propose a novel respiratory phase sorting method for 4D imaging based on optical surface imaging information, as an alternative solution to existing approaches based on the FM, diaphragm segmentation, pressure detectors or infrared blocks; 2. Evaluate the accuracy of the proposed method, in terms of the estimated breathing frequency and the quality of the reconstructed 4D CBCTs, using the diaphragm-based results as reference. The diaphragm-based method was used as a reference because: 1) The diaphragm muscle partially initiates and forms the respiratory pattern hence their correlations are physiologically oriented; 2) It is of good contrast with lungs and can be easily segmented on most image modalities; 3) The reliability of this internal anatomic marker has been well demonstrated [12], and has been adopted clinically in 4D CBCT respiratory phase sorting such as the Amsterdam Shroud (A-S) method [13].

2. Materials and methods

2.1. Data simulation

2.1.1. CBCT projections

Based on the geometric parameters of Varian kV CBCT system (Table 1), 1320 image projections of various gantry angles were simulated for CBCT image reconstruction, using 4D eXtended CArdiac-Torso (XCAT) (male) digital phantom on the Microsoft Windows 10 operating system with two NVIDIA GeForce RTX 3090 graphics cards. XCAT is a computerized model developed for biomedical imaging research, providing parameterized virtual patients with highly detailed and flexible normal or abnormal anatomies. Various respiratory motions or patterns can be simulated for research purposes. Functions of the XCAT include voxelization, simulating regional motion, modeling lesions, creating anatomical variations, and outputting motion vectors from the phantom etc. [14,15].

2.1.2. Surface point cloud extracted from simulated OSI data

To simulate the camera-captured OSI data synchronized to the 1320 CBCT projections of various respiratory phases, threshold segmentation was performed on the 4D images of XCAT phantom to acquire the body surface using MATLAB. Benefit from the natural image contrast between the air and patient, the external body contour can be well defined by a cutoff pixel value calculated through Otsu method [16]. To be consistent with the OSI data format, the segmented body surface was converted to a point cloud form, which is a data set of points in a coordinate system including three-dimensional spatial coordinates X, Y, Z, color, classification value, intensity value, and time, etc. The conversion to point cloud data was performed using Open3D module in Python. The ball pivoting method in Open3D module was called for triangle meshing, where the radius of the balls was determined by the average distance of the closest neighbor points. The simulation used the X, Y, Z information of the body surface data and arranged it from the upper left corner to the lower right corner. As an example of feasibility demonstration, a square region-of-interest (ROI) of 32 pixels × 32 pixels in size was selected at the chest-abdominal region for respiratory signal extraction.

2.2. *Respiratory signal extraction*

The motion signals were obtained from the diaphragm and OSI images respectively, to arrange the projection images into 10 phases based on the amplitude of inhalation and exhalation. The inspiratory (In) state was divided into In 0%, In 20%, In 40%, In 60%, In 80%, and In 100%. The expiratory state (Out) was divided into Out 20%, Out 40%, Out 60%, and Out 80% [17]. The end of inspiration (EOI) and the end of expiration (EOE) phases were defined as In 100% and In 0% phases respectively.

2.2.1. *Diaphragm-based breathing phase sorting method*

The well-established diaphragm-based breathing phase sorting method was used as a reference. To increase the contrast between the lung and liver, the projection images were filtered and then first order differential transformed. The finite difference along the horizontal direction was calculated to enhance the edge details. In accordance with Amsterdam Shroud (A-S) method which has been commercially and clinically used in diaphragm-based phase sorting [13], the enhanced projection was collapsed horizontally into a column to form a one-dimensional vector, and was subsequently put into a two-dimensional matrix. The two latitudes reflect the rotation angle (i.e., the data acquisition time) and the longitudinal spatial position of the detector, respectively. After alignment, the respiratory motion amplitude was calculated as the offset of each vector in the matrix relative to the first vector, based on Principal Component Analysis (PCA) method [18]. The respiratory motion signal was smoothed using Gaussian noise reduction and normalized to one. Fig. 1 is a flowchart of the whole

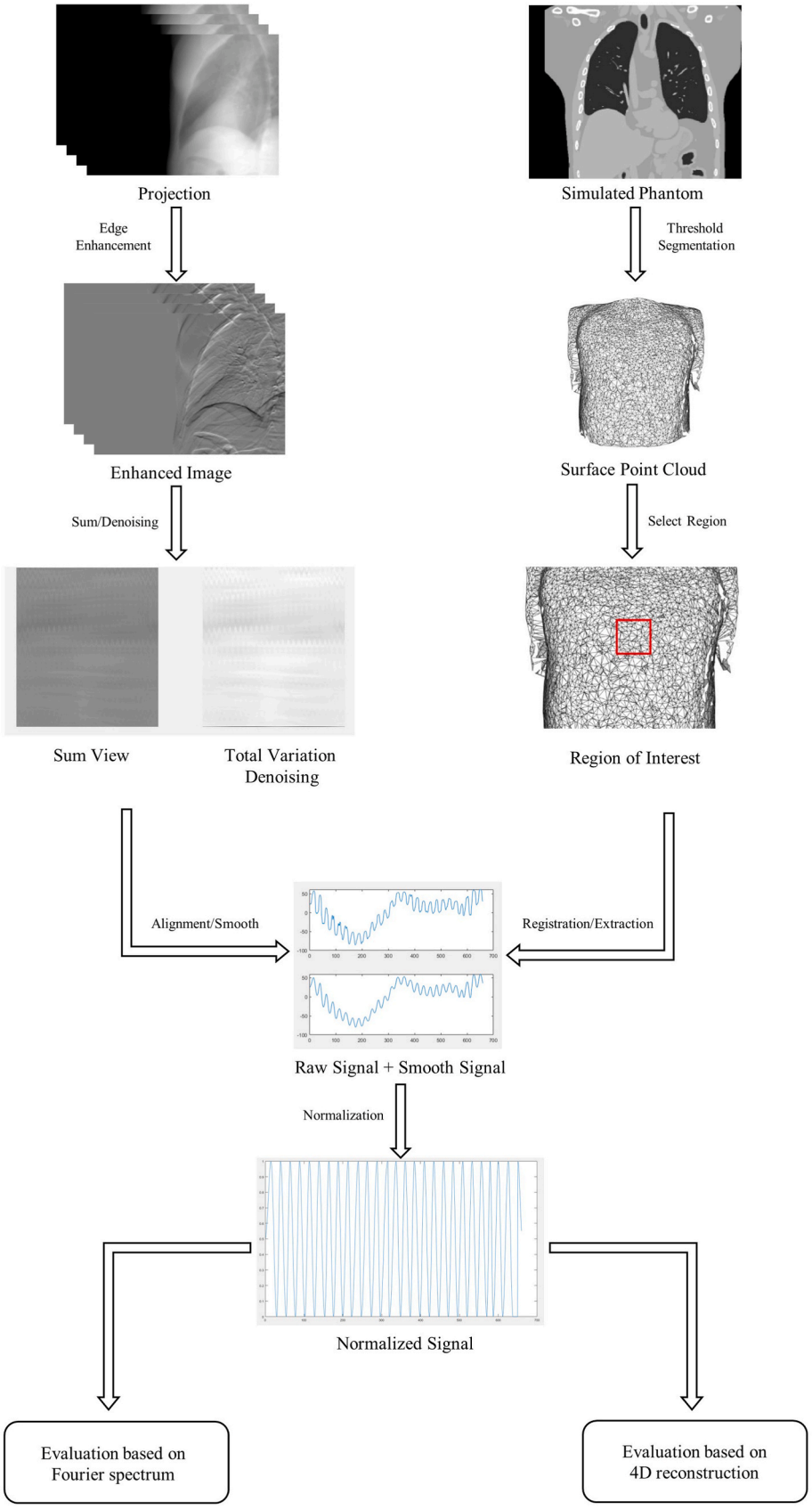

Fig. 1. Flowchart of respiratory signal extraction based on optical surface and diaphragm respectively. The quantitative evaluation was performed using Fourier spectrum and reconstructed 4D images respectively.

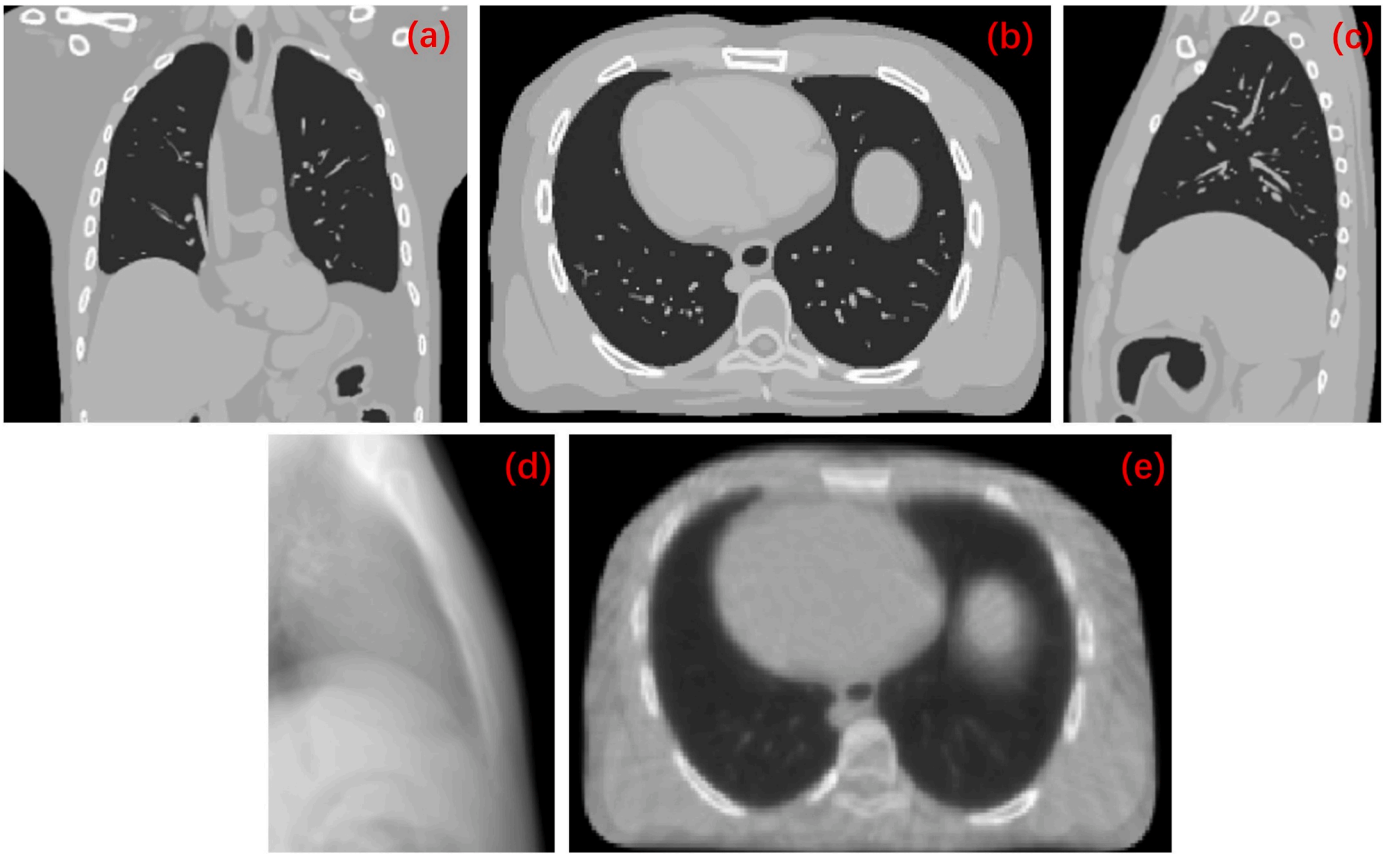

Fig. 2. (a–c) The coronal, sagittal and transverse views of XCAT CT phantom; (d) The simulated projection at gantry angle 0°; (e) The average cone-beam CT reconstructed from all projections of various respiratory phases.

process.

2.2.2. OSI-based phase sorting method

Based on the simulated OSI data, the initial phase (EOE) was selected as the reference, to which the surface point clouds of other phases were registered using a Gaussian mixture model for point cloud data registration [19]. It is a non-rigid point set registration algorithm with efficient noise suppression, which uses Gaussian distribution to represent the input point set mixture model. The point set registration problem was reformulated as the registration problem of two Gaussian mixture models (GMM). The L2 distance based on two Gaussian mixtures was calculated by minimizing the statistical difference between two Gaussian mixtures. The L2 distance is obtained through multiple iterations, and the result is fed back to registration to obtain the optimal solution. Compared with other point cloud registration algorithms such as Iterative Closest Point (ICP) method, GMM is not only intuitive and facile to implement, but also exhibits inherent statistical robustness.

The displacement of all points between the registered deformed ROI and the reference ROI was calculated. The displacement vector field does not only contain a comprehensive description of adequate spatial and temporal surface information, but also implies periodic components reflecting respiratory movements. However, dimension reduction needs to be performed to extract the respiratory signals effectively. PCA has been demonstrated as an effective approach in diaphragm-based respiratory signal extraction [13], which was also applied to the OSI method this study. The raw signal of the OSI was represented as the first principal component (PC1). Gaussian noise reduction was performed before the smoother curves were used for normalization.

2.2.3. Respiratory signal evaluation

In order to assess the consistency of motion signals extracted from the OSI and diaphragm images, the Fast Fourier Transform (FFT) of the normalized signal was evaluated, and the extracted spectrum was used to represent the respiratory cycle. FFT method was used to standardize the period signal waveforms acquired from different methods and structures.

2.3. Agreement evaluation based on 4DCBCT images

2.3.1. 4DCBCT reconstruction

Filtered Back Projection (FBP) reconstruction algorithm and iterative reconstruction algorithm are widely used for CT image reconstruction. FBP utilizes mathematical filters in the back projection step, allowing high-speed computation of the image reconstruction from projection data. The Feldkamp-Davis-Kress (FDK) algorithm is a typical FBP method. Iterative reconstruction algorithms generate and update three-dimensional volumetric data by comparing the estimated with the measured projections, and the Maximum Likelihood Expectation Maximization (MLEM) algorithm is a typical iterative reconstruction algorithm. Using a specially constructed likelihood function as the objective function for iteration [20], MLEM can suppress image noise more effectively than FDK algorithm based on sparse projection data. This study used MLEM algorithm to reconstruct 4D CBCT images based on the diaphragm and surface signals respectively. The FBP reconstructions were set as the estimated data and 50 iterations were conducted.

2.3.2. Image based agreement evaluation of respiratory signals

The image consistency based on two phase sorting methods was quantitatively assessed using Root Mean Square Error (RMSE), Structural Similarity Index (SSIM), and Peak Signal-To-Noise Ratio (PSNR) metrics. Their formulas can be found in references [21–23]. According to their definitions, lower RMSE indicates smaller image error, the SSIM

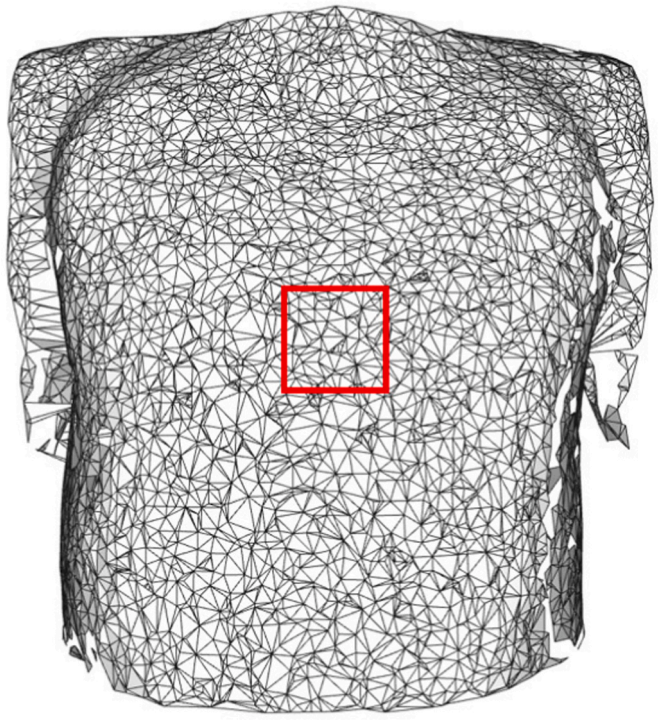

Fig. 3. An optical surface image in point cloud form simulated from body segmentation of XCAT phantom. The red square indicates the selected region of interest (32 pixels × 32 pixels) for respiratory signal extraction.

value closer to 1 suggests better consistency between the two images, and the larger PSNR values indicate better image quality and consistency [24].

3. Results

3.1. Simulated images

Fig. 2 shows examples of the XCAT-generated CT images (a-c), a simulated projection (d) and the reconstructed average CBCT images of all respiratory phases (e) respectively. The average CBCT was reconstructed from all 1320 projections using MLEM algorithm.

Fig. 3 shows a simulated optical surface image in point cloud form, on which a square ROI was selected for respiratory signal extraction.

3.2. Respiratory signals

Using discrete FFT, the respiratory motion signals in frequency domain were successfully acquired based on diaphragm images and OSI. The maximum amplitude on the spectrogram indicating the largest component proportion was used as the frequency of the respiratory motion. Fig. 4 compares the results of the discrete FFT of the two signals, where the frequency discrepancy between the OSI signal (0.251 Hz) and the diaphragm signal (0.232 Hz) was 0.019 Hz.

3.3. Evaluation based on 4D images

Sorted by the motion signals extracted from the diaphragm and OSI respectively, 4D images of 10 respiratory phases were successfully reconstructed using MLEM algorithm. As examples, Fig. 5 displays the transverse, coronal and sagittal views of the EOE and EOI phases. The consistency between the diaphragm- and surface-based images was assessed quantitatively in Table 3 in terms of RMSE, SSIM and PSNR.

4. Discussion

The breathing signal frequencies between diaphragm and OSI methods were mostly consistent, although minor difference of 0.019Hz was observed between the peak frequencies in the Fourier spectrums. This discrepancy might be ascribable to the complex nature of respiratory motion, which is jointly determined by the diaphragm and skeletal

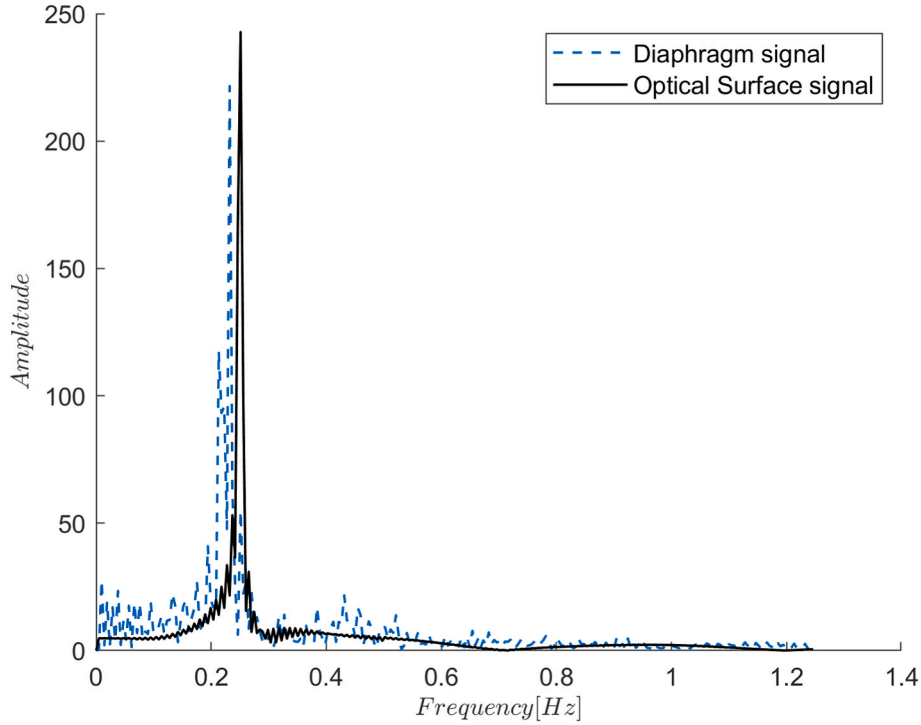

Fig. 4. Frequency of amplitude extracted from diaphragm images and optical surface respectively.

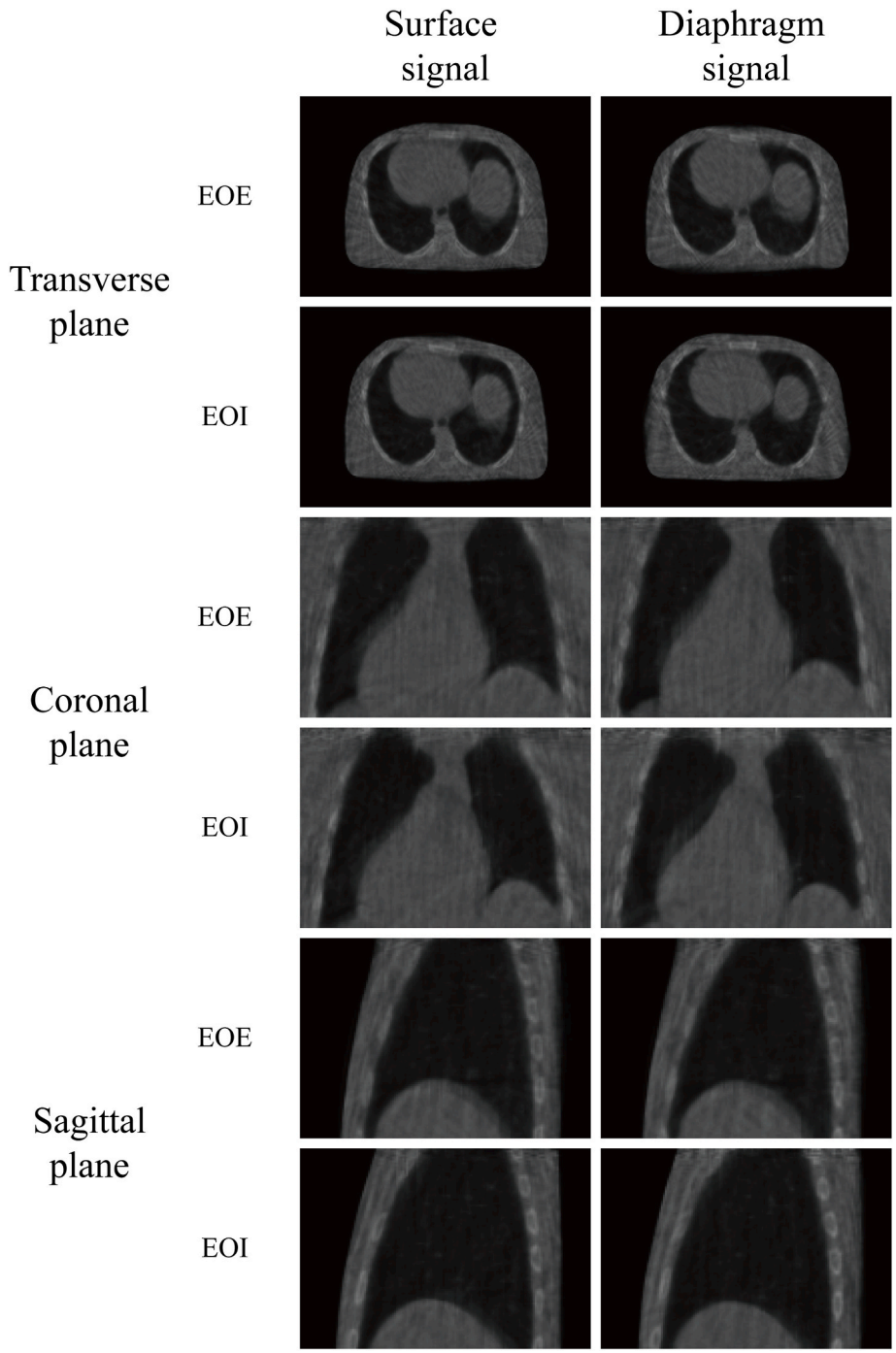

Fig. 5. 4D images reconstructed using surface signals (in the left column) and diaphragm signals (in the right column) for transverse, coronal and sagittal planes. EOI = end of inspiration; EOE = end of expiration.

muscles at the chest-abdominal region. Therefore, the surface motion is partially voluntary rather than passively determined by the diaphragm, yielding similar but not identical Fourier spectrums. Another possible explanation is that the PC1s showed slightly different main motions in diaphragm (Superior-Inferior curve) and in surface (Anterior-Posterior curve) respectively.

High consistency was also observed between the 4D images reconstructed from the two methods, as shown in Fig. 5 and Table 3. For instance, the minimum PSNR value reported in Table 3 was 36.845 ± 1.322, higher than the threshold of 35 providing satisfactory image quality and consistency with reference as suggested in the literatures [25,26]. On the other hand, the proposed surface-based method can be superior to the reference in some application scenarios, such as when the imaging FOV cannot or should not cover the diaphragm. The OSI method does not require extra imaging projection and radiation dose during gated treatment, and is more compatible to various systems such as CT, CBCT, MRI, and respiration-gated treatment systems, etc.

To sort the images to various respiratory phases effectively, the temporal resolution of OSI should not be lower than the frequency of kV projection acquisition. As reported previously in studies [27–29], the acquisition rate of 4D CBCT was between 5.5 and 15 frames per second (fps). The temporal resolution of the commercial depth camara used for OSI acquisition is not lower than 30 frames per second (such as the Intel RealSense D345 camera), which is more than competent to support the

Table 3
Consistency of 4D images reconstructed using the diaphragm and surface motion signals in terms of RMSE, SSIM and PSNR. The results are displayed as mean ±1SD of 80 transverse, 100 coronal and 120 sagittal planes respectively.

Phase	Plane	RMSE	SSIM	PSNR
In 0% (EOE)	Transverse	1.657 ± 0.368	0.967 ± 0.007	40.501 ± 1.737
	Coronal	1.464 ± 0.104	0.972 ± 0.003	41.532 ± 1.464
	Sagittal	1.479 ± 0.297	0.974 ± 0.008	41.553 ± 1.910
In 40%	Transverse	1.572 ± 0.217	0.970 ± 0.008	41.124 ± 1.391
	Coronal	1.374 ± 0.100	0.974 ± 0.001	42.253 ± 0.689
	Sagittal	1.407 ± 0.199	0.975 ± 0.005	42.043 ± 1.086
In 100% (EOI)	Transverse	1.686.±0.278	0.969 ± 0.008	40.535 ± 1.539
	Coronal	1.422 ± 0.089	0.973 ± 0.001	41.605 ± 0.534
	Sagittal	1.489 ± 0.238	0.973 ± 0.007	41.401 ± 1.496
Out 40%	Transverse	1.622 ± 0.297	0.967 ± 0.009	40.545 ± 1.502
	Coronal	1.358 ± 0.048	0.973 ± 0.001	41.907 ± 0.448
	Sagittal	1.383 ± 0.202	0.975 ± 0.006	41.982 ± 1.557
Out 80%	Transverse	1.560 ± 0.285	0.969 ± 0.007	40.501 ± 1.175
	Coronal	1.358 ± 0.040	0.974 ± 0.001	42.055 ± 0.317
	Sagittal	1.399 ± 0.229	0.965 ± 0.005	41.560 ± 1.021

EOI = end of inspiration; EOE = end of expiration; RMSE = Root Mean Square Error; SSIM=Structural Similarity Index; PSNR=Peak Signal-To-Noise Ratio. Higher image consistency can be suggested by lower RMSE, SSIM value closer to 1, or larger PSNR values respectively.

feasibility of the proposed OSI-based respiratory phase sorting method.

In addition to the methods using internal markers, surrogate signals collected using external devices were used for phase sorting and respiratory gating in both imaging and treatment systems. One example is the Real-time Position Management system (RPM, Varian Medical Systems, Palo Alto, CA), which tracks the anterior-posterior (AP) displacement of a block placed on the chest-abdominal region using an infrared camera [30]. Another external technique is based on the pressure change detected by the sensor attached to the patient surface [31]. Compared with these existing contact type external methods using block tracking or pressure detection, the proposed surface image-based approach provided an alternative solution for image phase sorting or respiratory gating treatment, without any contact type accessories attached to the patient body.

The synchronization of OSI data with 4D imaging also combines their complementary advantages for the application to accurate radiotherapy. For instance, by acquiring the pretreatment 4D CBCT and optical surface data simultaneously after patient setup, the real-time surface motion during the treatment can be associated with visible 4D internal anatomies that is most adjacent to the treatment time [32], without extra imaging dose, contact type accessories or expensive MRI integration.

This study is limited by its simulation design. In addition, the optimal location and size of ROI selection on the OSI is worth additional research. These problems will be investigated further based on real patient data in the future.

5. Conclusions

To improve the precision of radiotherapy, this simulation work proposed a new method of respiratory phase sorting for 4-dimensional imaging based on optical surface data. Quantitative evaluation based on both amplitude frequency and 4D image quality demonstrated good consistency between the proposed method and the reference method using the diaphragm as an internal marker. The potential advantages of the proposed approach include: 1) The non-ionizing OSI does not increase the radiation risk of patients but provides high temporal and spatial resolution. 2) It is non-invasive and non-contact, improving patients' comfort and clinical convenience. Surgery related infection and clinical contraindications can be minimized. 3) It is applicable to broader anatomic regions, especially when the diaphragm cannot or should not be covered in the imaging field. 4) It is less expensive but more compatible with other treatment and imaging systems, providing better cost-effectiveness and flexibility in image-guided radiotherapy.

Declaration of competing interest

The authors declare that they have no known competing financial interests or personal relationships that could have appeared to influence the work reported in this paper.

Acknowledgment

This work was jointly supported by Beijing Natural Science Foundation (Z210008); National Natural Science Foundation of China (12275012); Science Foundation of Peking University Cancer Hospital (2021–1, PY202305, PY202306); Peking University Emerging Engineering Interdisciplinary Project/the Fundamental Research Funds for the Central Universities (PKU2022XGK006); Peking University Health Science Center Medical Education Research Funding Project (2020YB34); an award from the UCL-PKU Strategic Partner Funding Scheme facilitated by UCL Global Engagement; the Wellcome/EPSRC Centre for Interventional and Surgical Sciences (WEISS) (203145/Z/16/Z); National Key R&D Program of China (2019YFF01014405); Open Project funded by Key Laboratory of Carcinogenesis and Translational Research, Ministry of Education/Beijing (2022 Open Project-2); Inner Mongolia Science & Technology Project Plan (2022YFSH0064).

AS would like to acknowledge support by the Wellcome/EPSRC Centre for Interventional and Surgical Sciences (WEISS) (203145/Z/16/Z).

This research was funded in part, by the Wellcome Trust [203145/Z/16/Z]. For the purpose of Open Access, the author has applied a CC BY public copyright licence to any Author Accepted Manuscript version arising from this submission.

The authors would like to thank Jamie McClelland, Yugang Wang, Catarina Isabel, Yuliang Huang, Hongxin Zhao and Zixuan Tian for their kind assistance.

References

[1] T. Harada, H. Shirato, S. Ogura, S. Oizumi, K. Yamazaki, S. Shimizu, R. Onimaru, K. Miyasaka, M. Nishimura, H. Dosaka-Akita, Real-time tumor-tracking radiation therapy for lung carcinoma by the aid of insertion of a gold marker using bronchofiberscopy, Cancer 95 (2002) 1720–1727, https://doi.org/10.1002/cncr.10856.

[2] S.S. Vedam, V.R. Kini, P.J. Keall, V. Ramakrishnan, H. Mostafavi, R. Mohan, Quantifying the predictability of diaphragm motion during respiration with a noninvasive external marker, Med. Phys. 30 (2003) 505–513, https://doi.org/10.1118/1.1558675.

[3] R.L. Ehman, M.T. McNamara, M. Pallack, H. Hricak, C.B. Higgins, Magnetic resonance imaging with respiratory gating: techniques and advantages, AJR Am. J. Roentgenol. 143 (1984) 1175–1182, https://doi.org/10.2214/ajr.143.6.1175.

[4] C. Saw, E. Brandner, R. Selvaraj, H. Chen, M. Saiful Huq, D. Heron, A review on the clinical implementation of respiratory-gated radiation therapy, Biomed. Imaging Interv. J. 3 (2007), https://doi.org/10.2349/biij.3.1.e40.

[5] C. Goldsmith, M.M. Green, B. Middleton, I. Cowley, A. Robinson, N.P. Plowman, P. M. Price, Evaluation of CyberKnife® fiducial tracking limitations to assist targeting accuracy: a phantom study with fiducial displacement, Cureus (2018), https://doi.org/10.7759/cureus.3523.

[6] N. Kothary, J.J. Heit, J.D. Louie, W.T. Kuo, B.W. Loo, A. Koong, D.T. Chang, D. Hovsepian, D.Y. Sze, L.V. Hofmann, Safety and efficacy of percutaneous fiducial

marker implantation for image-guided radiation therapy, J. Vasc. Intervent. Radiol. 20 (2009) 235–239, https://doi.org/10.1016/j.jvir.2008.09.026.
[7] P. Freislederer, V. Batista, M. Öllers, M. Buschmann, E. Steiner, M. Kügele, F. Fracchiolla, S. Corradini, M. de Smet, F. Moura, S. Perryck, F. Dionisi, D. Nguyen, C. Bert, J. Lehmann, ESTRO-ACROP guideline on surface guided radiation therapy, Radiother. Oncol. 173 (2022) 188–196, https://doi.org/10.1016/j.radonc.2022.05.026.
[8] J.D.P. Hoisak, T. Pawlicki, The role of optical surface imaging systems in radiation therapy, Semin. Radiat. Oncol. 28 (2018) 185–193, https://doi.org/10.1016/j.semradonc.2018.02.003.
[9] C. Jenkins, L. Xing, A. Yu, Using a handheld stereo depth camera to overcome limited field-of-view in simulation imaging for radiation therapy treatment planning, Med. Phys. 44 (2017) 1857–1864, https://doi.org/10.1002/mp.12207.
[10] R.L. Siegel, K.D. Miller, A. Jemal, Cancer statistics, CA A Cancer J. Clin. 70 (2020) 7–30, https://doi.org/10.3322/caac.21590, 2020.
[11] J.-P. Pouget, A.G. Georgakilas, J.-L. Ravanat, Targeted and off-target (bystander and abscopal) effects of radiation therapy: redox mechanisms and risk/benefit Analysis, Antioxidants Redox Signal. 29 (2018) 1447–1487, https://doi.org/10.1089/ars.2017.7267.
[12] Q. Zhang, A. Pevsner, A. Hertanto, Y.-C. Hu, K.E. Rosenzweig, C.C. Ling, G. S. Mageras, A patient-specific respiratory model of anatomical motion for radiation treatment planning, Med. Phys. 34 (2007) 4772–4781, https://doi.org/10.1118/1.2804576.
[13] M. Chao, J. Wei, T. Li, Y. Yuan, K.E. Rosenzweig, Y.-C. Lo, Robust breathing signal extraction from cone beam CT projections based on adaptive and global optimization techniques, Phys. Med. Biol. 61 (2016) 3109–3126, https://doi.org/10.1088/0031-9155/61/8/3109.
[14] W.P. Segars, G. Sturgeon, S. Mendonca, J. Grimes, B.M.W. Tsui, 4D XCAT phantom for multimodality imaging research, Med. Phys. 37 (2010) 4902–4915, https://doi.org/10.1118/1.3480985.
[15] W.P. Segars, B.M.W. Tsui, J. Cai, F.-F. Yin, G.S.K. Fung, E. Samei, Application of the 4-D XCAT phantoms in biomedical imaging and beyond, IEEE Trans. Med. Imag. 37 (2018) 680–692, https://doi.org/10.1109/TMI.2017.2738448.
[16] N. Otsu, A threshold selection method from gray-level histograms, IEEE Trans Syst Man Cybern 9 (1979) 62–66, https://doi.org/10.1109/TSMC.1979.4310076.
[17] J. Liu, T. Lin, J. Fan, L. Chen, R. Price, C.-M.C. Ma, Evaluation of the combined use of two different respiratory monitoring systems for 4D CT simulation and gated treatment, J. Appl. Clin. Med. Phys. 19 (2018) 666–675, https://doi.org/10.1002/acm2.12434.
[18] H. Yan, X. Wang, W. Yin, T. Pan, M. Ahmad, X. Mou, L. Cerviño, X. Jia, S.B. Jiang, Extracting respiratory signals from thoracic cone beam CT projections, Phys. Med. Biol. 58 (2013) 1447–1464, https://doi.org/10.1088/0031-9155/58/5/1447.
[19] Bing Jian, B.C. Vemuri, Robust point set registration using Gaussian mixture models, IEEE Trans. Pattern Anal. Mach. Intell. 33 (2011) 1633–1645, https://doi.org/10.1109/TPAMI.2010.223.
[20] D.H. Lee, Y.S. Kim, S.H. Choi, H.H. Lee, H.J. Kim, Feasibility Study for 3D Cone-Beam Computed Tomography Reconstruction with Few Projection Data Using MLEM Algorithm with Total Variation Minimization, 2015, pp. 66–69, https://doi.org/10.1007/978-3-319-19387-8_17.
[21] T. Chai, R.R. Draxler, Root mean square error (RMSE) or mean absolute error (MAE)? – Arguments against avoiding RMSE in the literature, Geosci. Model Dev. (GMD) 7 (2014) 1247–1250, https://doi.org/10.5194/gmd-7-1247-2014.
[22] L. Zhou, J.D. Schaefferkoetter, I.W.K. Tham, G. Huang, J. Yan, Supervised learning with cyclegan for low-dose FDG PET image denoising, Med. Image Anal. 65 (2020), 101770, https://doi.org/10.1016/j.media.2020.101770.
[23] Z. Wang, A.C. Bovik, H.R. Sheikh, E.P. Simoncelli, Image quality assessment: from error visibility to structural similarity, IEEE Trans. Image Process. 13 (2004) 600–612, https://doi.org/10.1109/TIP.2003.819861.
[24] Z. Jiang, Y. Chen, Y. Zhang, Y. Ge, F.-F. Yin, L. Ren, Augmentation of CBCT reconstructed from under-sampled projections using deep learning, IEEE Trans. Med. Imag. 38 (2019) 2705–2715, https://doi.org/10.1109/TMI.2019.2912791.
[25] D.R. Bull, F. Zhang, Digital picture formats and representations, in: Intelligent Image and Video Compression, Elsevier, 2021, pp. 107–142, https://doi.org/10.1016/B978-0-12-820353-8.00013-X.
[26] Y. Liu, X. Chen, J. Zhu, B. Yang, R. Wei, R. Xiong, H. Quan, Y. Liu, J. Dai, K. Men, A two-step method to improve image quality of CBCT with phantom-based supervised and patient-based unsupervised learning strategies, Phys. Med. Biol. 67 (2022), 084001, https://doi.org/10.1088/1361-6560/ac6289.
[27] A.P. Santoso, K.H. Song, Y. Qin, S.J. Gardner, C. Liu, I.J. Chetty, B. Movsas, M. Ajlouni, N. Wen, Evaluation of gantry speed on image quality and imaging dose for 4D cone-beam CT acquisition, Radiat. Oncol. 11 (2016) 98, https://doi.org/10.1186/s13014-016-0677-8.
[28] Y. Zhang, F.-F. Yin, T. Pan, I. Vergalasova, L. Ren, Preliminary clinical evaluation of a 4D-CBCT estimation technique using prior information and limited-angle projections, Radiother. Oncol. 115 (2015) 22–29, https://doi.org/10.1016/j.radonc.2015.02.022.
[29] S.A. Yoganathan, K.J. Maria Das, S. Mohamed Ali, A. Agarwal, S.P. Mishra, S. Kumar, Evaluating the four-dimensional cone beam computed tomography with varying gantry rotation speed, Br. J. Radiol. 89 (2016), 20150870, https://doi.org/10.1259/bjr.20150870.
[30] J.R. McClelland, S. Hughes, M. Modat, A. Qureshi, S. Ahmad, D.B. Landau, S. Ourselin, D.J. Hawkes, Inter-fraction variations in respiratory motion models, Phys. Med. Biol. 56 (2011) 251–272, https://doi.org/10.1088/0031-9155/56/1/015.
[31] M. Chu, T. Nguyen, V. Pandey, Y. Zhou, H.N. Pham, R. Bar-Yoseph, S. Radom-Aizik, R. Jain, D.M. Cooper, M. Khine, Respiration rate and volume measurements using wearable strain sensors, NPJ Digit Med 2 (2019) 8, https://doi.org/10.1038/s41746-019-0083-3.
[32] Y. Huang, Z. Dong, H. Wu, C. Li, H. Liu, Y. Zhang, Deep learning-based synthetization of real-time in-treatment 4D images using surface motion and pretreatment images: a proof-of-concept study, Med. Phys. 49 (2022) 7016–7024, https://doi.org/10.1002/mp.15858.